Absorption of a nanosecond laser pulse by a picosecond laser-induced preformed aluminum plasma

Aurélien Favre, Vincent Morel, Arnaud Bultel, Gilles Godard, Saïd Idlahcen, Christian Grisolia

Absorption of a nanosecond laser pulse by a picosecond laser-induced preformed aluminum plasma

Aurélien Favre[a], Vincent Morel[a], Arnaud Bultel[a], Gilles Godard[a], Said Idlahcen[a], Christian Grisolia[b]

[a] *CORIA, UMR CNRS 6614, 76801 Saint-Etienne du Rouvray Cedex, FRANCE*
[b] *IRFM, CEA Cadarache, 13801 Saint-Paul-lez-Durance, FRANCE*

Abstract

The LIBS (Laser-Induced Breakdown Spectroscopy) method has already demonstrated its reliability and its robustness in many situations for the multi-elemental composition determination of samples. However, certain conditions prevent a totally satisfactory determination. For instance, the method is weakly efficient to measure with accuracy the light elements concentration in metallic matrices. Since the laser pulse used to produce the plasma contributes to its heating, using an additional pulse (double pulse configuration) provides the increase in electron temperature and density without additional ablation. A better signal-to-noise ratio and a lower limit of detection can be reached. The present paper reports the results of different experiments performed to quantify the modifications induced (1) on the electron density by the second laser pulse in a preformed aluminum plasma, and (2) on the second laser pulse itself. The related experiments have been done in the case where the plasma is produced by a picosecond laser pulse and the second laser pulse is of the nanosecond type. The electron density reaches a maximum resulting from the total ionization of the aluminum plasma volume irradiated by the second laser pulse.

Email address: aurelien.favre@coria.fr (Aurélien Favre)
URL: http://www.coria.fr (Aurélien Favre)

Key words: Laser-induced plasmas, LIBS, Aluminum, Double-pulse, Picosecond, Nanosecond, Absorption, Inverse Bremsstrahlung, Multiphoton ionization

1. Introduction

The Laser-Induced Breakdown Spectroscopy (LIBS) is based on the irradiance of a sample (for instance solid) to be analyzed by a laser pulse above a threshold of $\sim 10^{13}$ W m^{-2} leading to the formation of a freely expanding plasma [1].

Two situations can be observed according to the density of free electrons inside the solid. If the material is dielectric, multiphoton ionization (MPI) contributes to the production of the first free electrons. Then, they absorb the laser light by Inverse Bremsstrahlung (IB) [2]. If free electrons exist in the sample, the MPI processes do not participate so much to the ionization of the plasma. Laser photons are absorbed by IB. In the two cases, the electron temperature T_e increases, which leads to the increase in the electron density n_e resulting from the enhancement of the collisional ionization (CI). The bonds between particles inside the sample are broken, the pressure reaches several 10^9 Pa [3] and the matter is strongly ejected from the resulting crater according to a hypersonic expansion regime [4]. The ablated material has a decreasing temperature during its expansion and contributes to a partial ionization of the components of the background gas crossed by the shockwave.

The temperature and density levels are high and allow the emission of light whose spectroscopic analysis is performed for LIBS. The light emission and therefore the collected signal radiance directly depend on the ablated mass [5]. The spectroscopic analysis shows that thermal equilibrium is reached owing to the elastic collisions at high electron density ($n_e > 10^{23}$ m^{-3}) [6]. This value of n_e coupled with the cooling of the plasma lead to a significant ionic recombination [7]. This impacts the feature

of the spectra mainly characterized by a continuum at early time and by ionic then atomic lines at longer time.

Due to its easy implementation, most of the LIBS applications are based on the use of a laser single pulse (SP). This explains why so many papers have been dedicated to such a configuration. However, the limit of detection of some elements is too high and should be reduced. Using a double pulse (DP) configuration can overcome a part of these limitations by increasing the electron temperature and density within the plasma. Despite its difficult implementation, this configuration represents a serious and seducing alternative.

DP configurations have been therefore tested in many situations. Most of the experimental setups are of the colinear type. This means that the two pulses belong to the same optical axis, systematically perpendicular to the sample. They use one [8] or two laser sources in ns/ns [9, 10, 11, 12, 13] or fs/ns [14, 15] configurations for the first/second pulse, respectively. They often use infrared radiation for the first pulse [9, 10, 11, 12, 13] and either infrared [9, 10, 11, 12, 15] or visible [13, 14] radiation for the second pulse. For colinear configurations, the use of optical fibres can be very useful [16]. For non colinear configurations, an angle of 90 degrees is considered, using one [14] or two [17] laser sources.

From a more fundamental point of view, detailed studies have been already performed to put into light the mechanism of interaction of the second pulse with the plasma produced by the first pulse. An important part of these studies has been focused on plasma experiments under water [18]. But most of them has been performed in a gaseous environment. A higher temperature level has been put forward to explain the change in the emitted light [19]. The morphology modifications have been also studied using shadowgraphy [20]. The influence of the second pulse on the ablation have been also characterized [21] as well as the one due to the background

gas [22]. An interesting review of these questions can be found in [23]. The DP configuration has been also studied from the modeling point of view [24].

The works cited above are focused on the improvement induced by the use of the second pulse in the framework of the LIBS technique. As colinear configurations are mainly implemented, the different delays between the two pulses open the question of the influence on the reported improvement of the additional ablation resulting from the partial transparency of the first laser pulse-induced plasma. Indeed, if the delay is sufficiently long to correspond to a too weak electron density, the second pulse reaches the sample despite its partial absorption by the plasma. Then an over-ablation takes place. The relative contribution of this second step of ablation and of the light absorption by the plasma in the enhancement of the relevant lines is difficult to estimate [25]. This prevents an optimization of the LIBS technique based on an unambiguous understanding of the underlying physics. In our opinion, in parallel with the technical verifications of the advantages of DP configurations in LIBS, a more fundamental study rather dedicated to the interaction between the second laser pulse and the plasma produced by the first laser pulse excluding any influence of the over-ablation has to be performed.

The present paper deals with this purpose from the experimental point of view. Since Aluminum is certainly the element mainly studied in laboratory laser-induced plasmas, Al samples have been used. They are irradiated first by a picosecond laser pulse to reduce as much as possible the interaction with the plasma in expansion. Then, a second laser pulse of the nanosecond type is used to increase n_e and T_e. The propagation axis of the second pulse is parallel to the sample to avoid any additional ablation when the time delay between the two pulses is increased. In the following, the experimental setup is described. The experiments are then reported. They have been performed to characterize the influence at given energy of the time delay

between the two pulses. The energy is kept constant to enable the cross comparison of the maximum electron density obtained after absorption. The dynamics of n_e is deduced from the spectroscopic analysis and correlated to the spectral absorptivity of the second laser pulse by the absorbing plasma.

2. Experimental setup

2.1. The "PLEIADES" platform

The experiments have been performed on the PLEIADES (Plasmas by LasEr IrADiations and their Experimental Studies) platform of the CORIA laboratory [26]. Its modularity allows the study of many kinds of samples irradiated in various ways. As discussed in Introduction, most of the DP experiments are based on two consecutive coaxial beams shifted in time [27] perpendicular to the sample. Due to the expansion of the plasma, a decrease in density takes place. As a result, the absorptivity decreases, which leads to an additional ablation. It is therefore impossible to evaluate unambiguously the influence of the energy absorbed by the plasma. To avoid this difficulty, a perpendicular configuration has been used on PLEIADES. The first pulse corresponds to an optical axis perpendicular to the Al sample that produces the ablation. The second pulse is parallel to the sample. Figure 1 displays the experimental setup where the first optical axis appears in red and the second optical axis appears in green. DURAL (alloy of 95 % Al, 4 % Cu, 0.5 % Mg and 0.5 % Mn) is used as sample for the experiments and is placed in air at atmospheric pressure on a central (xyz)-stage holder.

The photons belonging to the first pulse are characterized by the wavelength $\lambda_1 = 1064$ nm. They are produced by an EKSPLA PL-2251 source delivering the energy $\bar{E}_1 = 20$ mJ over the pulse duration $\tau_1 = 30$ ps. Its standard deviation σ_{E_1}

does not exceed 1 %. The laser beam with the quality factor $M_1^2 \approx 2$ is focused on the aluminum sample using a plano-convex lens of $f_1 = 125$ mm as focal length. The beam diameter at $1/e^2$ is $2\omega_1 = 5$ mm before the lens. Its diameter on the sample is then $2\omega_1' = 2M_1^2 \frac{\lambda_1 f_1}{\pi \omega_1} \approx 70$ μm. The mean fluence on the sample is then $F_1 = \frac{\bar{E}_1}{\pi \omega_1'^2} \approx 5$ MJ m^{-2}. The second pulse is produced by a Q-SMART 450 laser source at the wavelength $\lambda_2 = 532$ nm according to a pulse duration of $\tau_2 = 5$ ns. The energy is $\bar{E}_2 = 15.2$ mJ with a standard deviation σ_{E_2} lower than 4 %. The second pulse is focused at the distance $H + 620$ μm from the sample surface on the first optical axis within the plasma produced by the first pulse using a $f_2 = 150$ mm focal length plano-convex lens according to figure 2. Before the lens, the second laser beam has a diameter $2\omega_2 = 6.5$ mm at $1/e^2$ of the central irradiance. With a beam quality factor $M_2^2 \approx 2$, its diameter within the plasma is $2\omega_2' = 2M_2^2 \frac{\lambda_2 f_2}{\pi \omega_2} \approx 30$ μm. This corresponds to a mean fluence of $F_2 = \frac{\bar{E}_2}{\pi \omega_2'^2} \approx 20$ MJ m^{-2}. With this value, we experimentally verify that the laser irradiance is lower than but very close to the breakdown threshold in ambient air. In this context, it is therefore possible to maximize the effect of the absorption on the plasma and to avoid as much as possible the formation of an air plasma when the aluminum plasma is not produced.

After collection by a plano-convex lens leading to a magnification $Ma = 1.6$, a part of the radiation produced by the plasma is analyzed using a Roper SCT-320 spectrometer (focal length $f = 320$ mm, aperture f/4.6, grating with 2400 grooves mm^{-1}, entrance slit width of $f_e = 10$ μm) equipped with a PI-MAX 4 camera (HBf emiCCD sensor with a maximum quantum efficiency around 450 nm and an elementary pixel size of 13×13 μm^2). Calibrations have been performed prior to the experiments. Therefore each image obtained on the sensor (1024 × 1024 pixels) of the camera can be converted in a three-dimensional (λ, z, L_λ) image where L_λ is the spectral radiance (cf. figure 2) taking into account the acquisition gate width of 20 ns.

In support of the spectroscopic analysis, the absorption of the second pulse is characterized using a high laser power and energy meter (Ophir Nova II) located on the second optical axis, beyond the plasma.

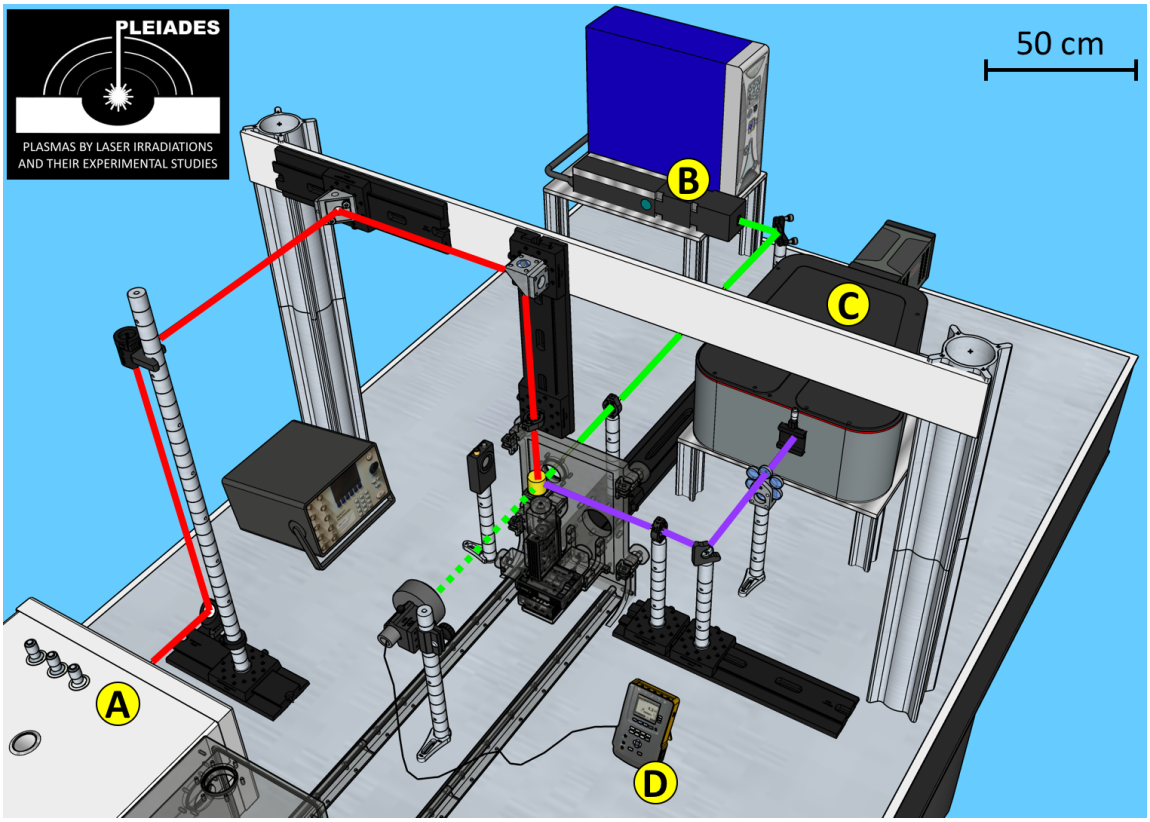

Figure 1: Schematic view of the platform PLEIADES.
The first laser source on the left produces infrared photons along the red axis. After focus, the plasma in yellow is generated on the Al sample placed on the central (xyz)-stage holder. The second laser source in the background produces visible photons along the green axis. They are focused in the plasma whose spectroscopic analysis is performed by the spectrometer on the purple axis.

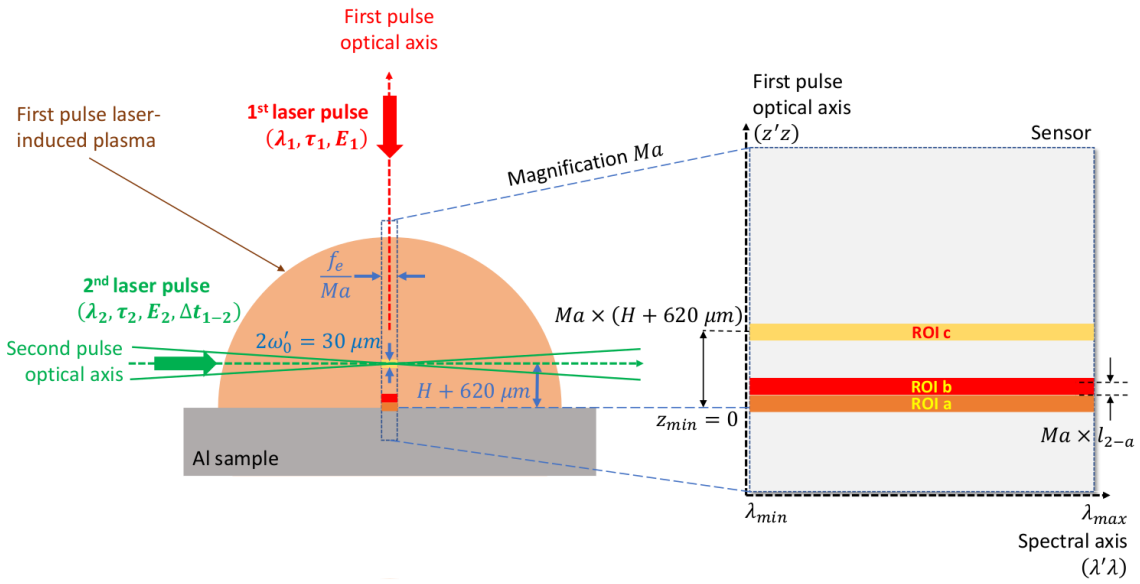

Figure 2: Relative sensor/plasma arrangement in the case where the second optical axis corresponds to the location of ROI c ($H = 1$ mm). When $H = 0$ mm, the distance betwen the upper border of the ROI a and the second optical axis is l_{2-a}.

2.2. Experimental protocol

In the following, three Regions of Interest (ROIs) of 50 rows of pixels on the sensor of the camera are used. This choice of 50 rows (corresponding to a height of $\delta = 400$ μm in the plasma) leads the second optical axis to be almost centered on ROI c when $H = 1$ mm (cf. figure 2) and to belong to ROI b when $H = 0$ mm. Except when a ROI coincides with the second optical axis, these 50 rows correspond to quasi uniformly emitting plasma regions. They enable to spatially estimate the characteristics of the plasma reheated by the second pulse. These ROIs denoted as ROI a, ROI b and ROI c in the following are located at the distance $z_a = -0.16$, $z_b = +0.24$ and $z_c = +1.36$ mm from the sample surface, respectively. The choice of these values has been guided by the features of the emission after a preliminary study not reported here.

The two parameters controlling the absorption of the second pulse by the plasma are

- the distance $H + 620$ μm between the surface of the sample and the optical axis of the second pulse,
- the time delay Δt_{1-2} between the two laser pulses.

The distance H is verified by imagery on the spectrometer used at the interferometric order 0 and is modified using the (xyz)-stage with an accuracy of 1 μm. Since the Rayleigh length of the first laser pulse is higher than H, changing the location of the sample does not significantly modify the irradiance. The time delay Δt_{1-2} is controlled by a pulse generator BNC 577 and is verified using a fast photodiode recording a signal proportional to the plasma radiance.

Table 1 summarizes the experimental conditions (H, Δt_{1-2}) considered for the spatial and temporal shifts between the laser pulses. They have been chosen to cover a wide range of situations. $H = 0$ mm corresponds to the second pulse appearing in

the ROI b. $H = 1$ mm is also tested. For each value of H, a time delay Δt_{1-2} of 150, 250 and 350 ns is considered. These conditions enable to estimate the influence of the initial n_e value on the absorption.

Experiment no j	1	2	3	4	5	6
H (mm)	0	0	0	1	1	1
Δt_{1-2} (ns)	150	250	350	150	250	350

Table 1: Tested experimental conditions.

3. Results

3.1. Observed spectra

Figures 3a, 3b and 3c display typical images obtained on the sensor in the vicinity of $\lambda = 396$ nm. This wavelength has been chosen since it corresponds to the Al I resonance doublet. These images have been obtained with an acquisition time t of 40, 380 and 480 ns for $(H, \Delta t_{1-2}) = (1$ mm, 350 ns). The plasma is formed by the first pulse on the sample at time $t = 0$. The spectra obtained from the ROIs are also displayed after conversion using the calibration. They correspond to the [390, 402] nm spectral range. The spectra exhibit lines whose dynamics strongly depends on the distance from the sample.

The well-known Al I resonance doublet is observed. The spectra displayed on figures 3b and 3c show that the concerned lines are not optically thin. Indeed, the upper level of the transition is the same for the two lines while the Einstein coefficient A_{ki} for spontaneous emission is almost in a ratio of 2 (cf. table 2). The intensity of the line at 396.152 nm should be twice the one of the line at 394.401 nm. Two contributions are responsible for this situation. First the plasma column heated

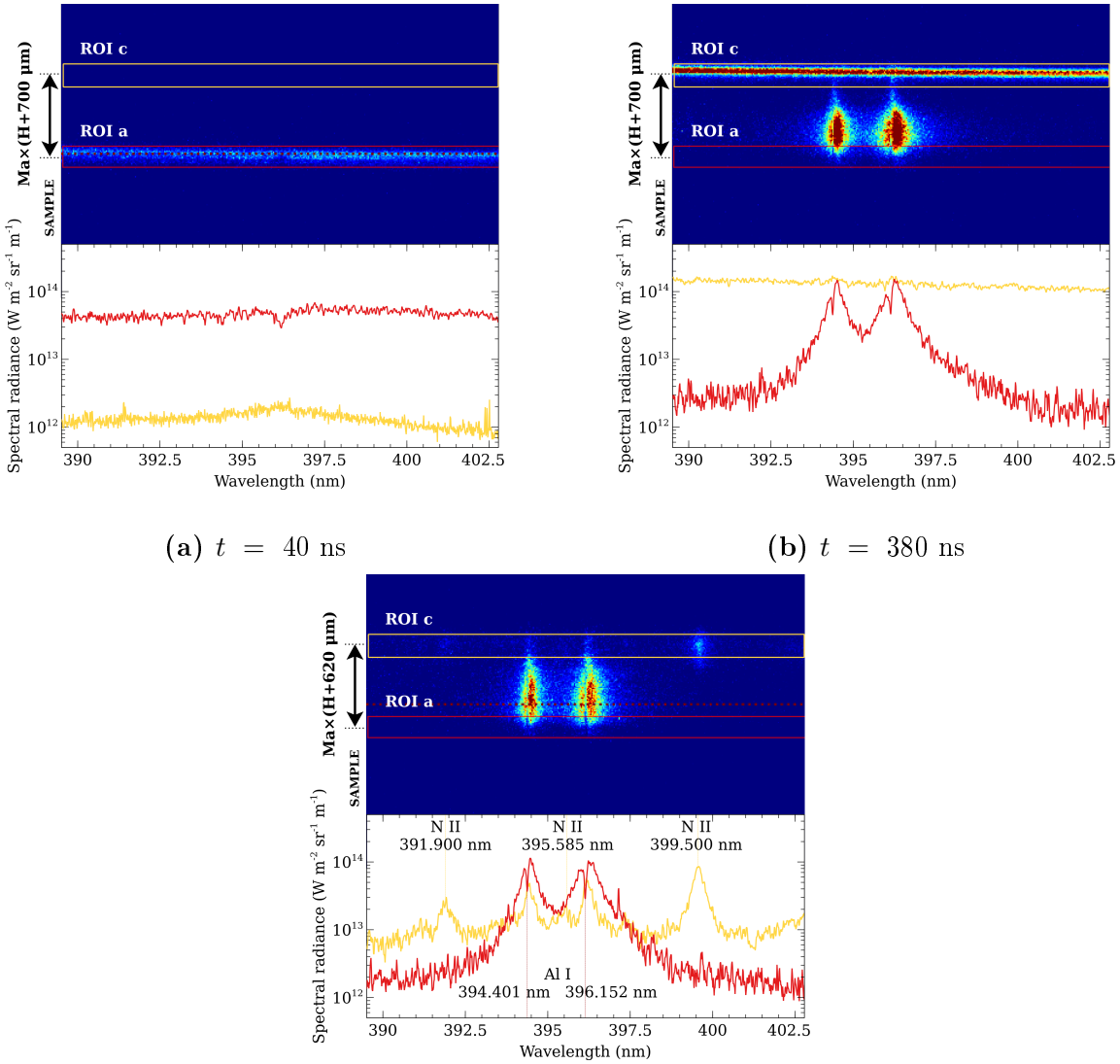

(a) $t = 40$ ns **(b)** $t = 380$ ns

(c) $t = 480$ ns

Figure 3: ROIs and associated spectra for $\lambda \sim 396$ nm at the acquisition time 40, 380 and 480 ns after the production of the plasma by the first pulse at $t = 0$. The plasma is reheated by the second pulse in the conditions $(H, \Delta t_{1-2}) = (1 \text{ mm}, 350 \text{ ns})$ of the experiment no 6. The red frames and spectra correspond to the plasma close to the sample (ROI a). The yellow frames and spectra correspond to the plasma reheated by the second pulse (ROI c).

by the second pulse self-absorbs the radiation. Second, the surrounding plasma containing Al atoms on their ground and first excited electronic states absorbs the radiation emitted at the center [28]. The relative estimate of these two contributions is not an easy task since it depends on the density of the lower level of the concerned transitions and on the crossed lengths.

Over the spectral range [390, 402] nm, some Al II transitions could be observed when the second pulse is implemented. The related lines correspond to the wavelength 390.068 nm ($E_k = 10.598$ eV, $g_k = 5$, $A_{ki} = 4.8 \times 10^5$ s^{-1}) and a multiplet with a mean wavelength of 399.6 nm ($E_k = 18.164$ eV, $g_k = 21$, $A_{ki} = 7.05 \times 10^6$ s^{-1}). Assuming the local thermodynamic equilibrium and neglecting any absorption process, the radiance ratio $I_{390.068}/I_{399.6}$ between these lines is 5.7 at 15 000 K, 1.3 at 20 000 K and 0.5 at 25 000 K. On the spectrum of the ROI c observed at $t = 480$ ns on figure 3c, the line around 399.5 nm could be ascribed to an Al II transition. In this case, since the previous radiance ratio is close to unity, the Al II transition should be observed at 390.068 nm. But, the spectrum does not exhibit any lines at this wavelength. This means that the line at around 399.5 nm cannot be ascribed to an Al II transition. If the line around 399.5 nm is due to a N II transition, other N II transitions should be observed. Two other N II transitions can indeed be observed on the [390, 402] nm spectral range. The first one corresponds to a wavelength of 391.900 nm and the second one corresponds to a wavelength of 395.585 nm. We can calculate the ratios in case of local thermodynamic equilibrium. The ratio $I_{391.900}/I_{399.500}$ equals 0.08 at 15 000 K, 0.12 at 20 000 K and 0.15 at 25 000 K. The ratio $I_{395.585}/I_{399.500}$ is equal to 0.1 for any value of T (the upper level of the transition corresponds to the same excitation energy). These values are in pretty good agreement with the yellow spectrum of figure 3c. We can conclude that the line around 399.5 nm is due to a N II transition as the other lines observed at 391.9 and 395.6 nm. Similar characteristics

have been already observed [29]. Except at 394.401 and 396.152 nm, aluminum does not radiate and the other lines are due to N II transitions. Table 2 lists the lines observed.

Line	Transition i - k	λ (nm)	A_{ki} (s^{-1})	g_i - g_k	E_i (eV) - E_k (eV)	ω_{ki} (nm)	Ref.
Al II	$3s3d\ ^3D_2$ - $3s4f\ ^3F^o_3$	358.707	2.09×10^8	5 - 7	11.847 - 15.302	1.60×10^{-2}	[30]
N II	$2s^22p3p\ ^1P$ - $2s^22p3d\ ^1P^o_1$	391.900	7.56×10^7	3 - 3	20.409 - 23.572	3.54×10^{-2}	[31]
Al I	$3s^23p\ ^2P^o_{1/2}$ - $3s^24s\ ^2S_{1/2}$	394.401	4.99×10^7	2 - 2	0.000 - 3.143	1.54×10^{-2}	[32]
N II	$2s^22p3s\ ^3P^o_1$ - $2s^22p3p\ ^1D_2$	395.585	1.21×10^7	3 - 5	18.466 - 21.600	2.77×10^{-2}	[31]
Al I	$3s^23p\ ^2P^o_{1/2}$ - $3s^24s\ ^2S_{1/2}$	396.152	9.85×10^7	4 - 2	0.014 - 3.143	1.54×10^{-2}	[32]
N II	$2s^22p3s\ ^1P^o_1$ - $2s^22p3p\ ^1D_2$	399.500	1.22×10^8	3 - 5	18.497 - 21.600	2.80×10^{-2}	[31]
Al II	$3p^2\ ^1D_2$ - $3s4p\ ^1P^o_1$	466.306	5.81×10^7	5 - 3	10.598 - 13.256	6.15×10^{-2}	[33]

Table 2: Lines and related transitions used along the present study. The given reference corresponds to the value of the full width at half maximum of the Stark effect-broadened line (at a reference electron density n_e^* of 10^{22} m^{-3} for the neutrals and of 10^{23} m^{-3} for the ions).

3.2. Direct analysis of the spectra

The spectra related to the Al I resonance doublet on figs 3b and 3c exhibit significant Stark broadening and shift. The wavelength corresponding to the emission without Stark shift is obtained by observing the depletion of the spectral radiance resulting from the absorption due to the plasma cold edge. This depletion corresponds to a ratio of 1/3 with respect to the maximum spectral radiance observed. The N II transition at 399.500 nm is observed on the ROI c spectrum at $t = 480$ ns only. At the same time, the resonance doublet lines are also observed at the same location. This means that (1) the expansion of the aluminum plasma is very rapid, (2) a mixing takes place with the background gas, (3) this mixing leads to the dissociation of N_2 and (4) the plasma is clearly reheated by the second pulse.

Figures 4 illustrates the evolution in time of the maximum spectral radiance from the ROIs a and c obtained for the lines of the aluminum resonance doublet lines and

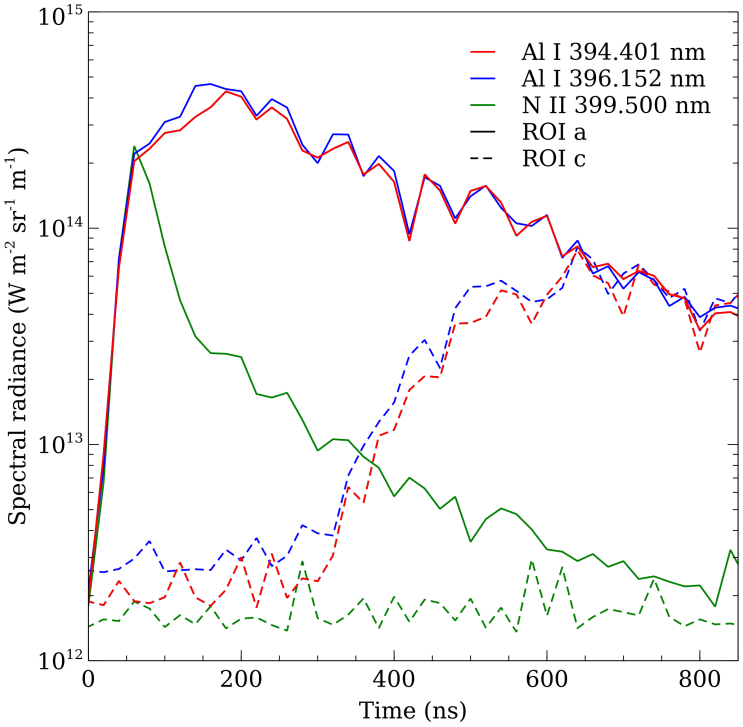

Figure 4: Time evolution of the spectral radiance at the wavelength of the Al I and N II transitions of figure 3 obtained without second pulse close to the sample's surface (ROI a, continuous lines) and ~ 1 mm above (ROI c, dashed lines).

for the ionic nitrogen line at 399.500 nm. This evolution has been obtained whithout irradiation by the second pulse. On this figure we can observe the sudden increase in the spectral radiance close to $t = 0$ resulting from the emission of the initial continuum. Around $t = 60$ ns, the lines start to appear in the spectra and the spectral radiance globally decreases. At $z_c = 1.36$ mm from the surface where ROI c is located, a very low value of the spectral radiance is observed, which corresponds to the noise. From $t' = 320$ ns, the spectral radiance starts to increase. This is due to the propagation of the plasma from the surface of the sample to this position. An estimate of the mean plasma speed over t' can therefore be deduced. This value is $z_c/t' = 4.2$ km s^{-1}. Thus, the expansion is hypersonic.

In the case where the second pulse is used, the previous temporal analysis can be also performed. Figures 5a, 5b and 5c display the related evolutions. Concerning the figures where $H = 0$ mm, a time delay between the increase in spectral radiance related to the Al I transitions for the ROIs a and b of around $t'' = 50$ ns can be logically ascribed to the plasma expansion close to $t = 0$. Beyond the estimate of the mean speed over t' mentioned previously, the initial speed can be obtained by the ratio $z_b/t'' = 4.8$ km s^{-1}. This speed is logically higher than the mean one since the propagation requires a significant momentum transfer to the background gas which brakes down the plasma expansion. This value of 4.8 km s^{-1} is in very good agreement with the value calculated by our model CoRaM-Al implemented in an Eulerian code [3] developed for similar situations, but with a lower energy $\bar{E}_1 =$ 10 mJ. The calculation is based on the following assumptions. The picosecond laser pulse produces the isochoric heating and ionization of the matter in the crater. Due to the strong increase in pressure, this matter hemispherically expands. Its contact with ambient atmosphere leads to momentum transfer according to a hypersonic regime which produces a strong shockwave freely expanding hemispherically. The mass,

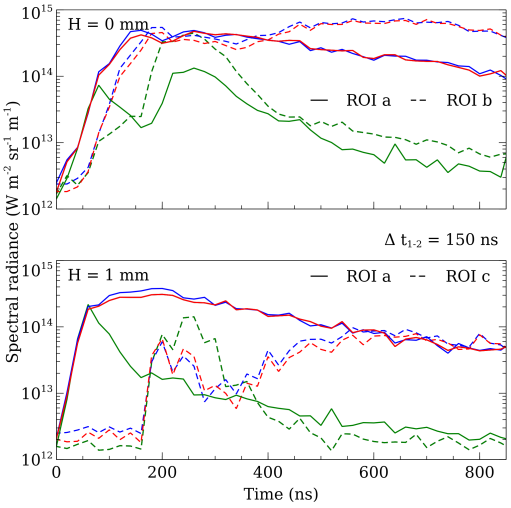

(a) Experiments 1 and 4.

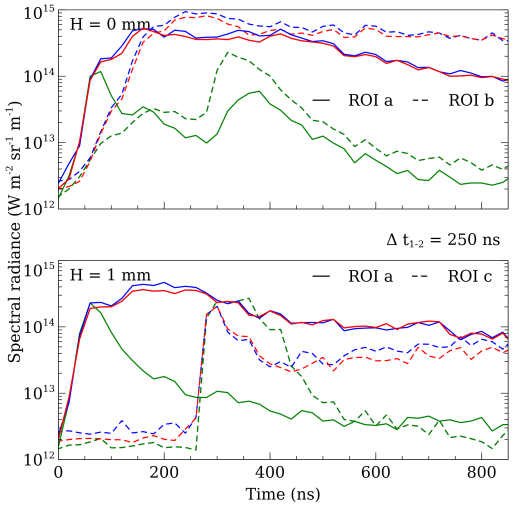

(b) Experiments 2 and 5.

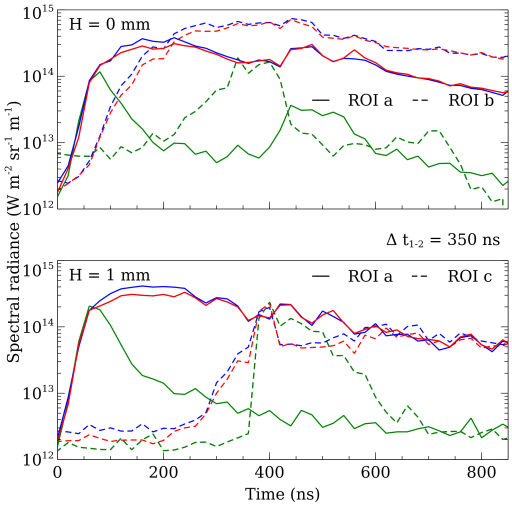

(c) Experiments 3 and 6.

Figure 5: Time evolution of the spectral radiance at the wavelength of the Al I and N II transitions obtained close to the sample's surface (ROI a, continuous lines) and over the ROI corresponding to the position of the second pulse (dashed lines, ROI b for $H = 0$ mm and ROI c for $H = 1$ mm) for the different values of Δt_{1-2} (colors similar to figure 4).

energy and momentum conservation equations are solved in time for these two layers separated by the contact surface assuming a homothetic speed field. In addition, the ejected matter is assumed out of thermodynamic equilibrium by considering the different excited states of aluminum. The input parameters are the energy delivered by the picosecond laser pulse $\bar{E}_1$, the ablated mass M and the pressure p_0 of the ambient gas. The model has been developed considering N_2 for this gas rather than air. All results related to the conditions $\bar{E}_1 = 10$ mJ, $M \sim 10^{-10}$ kg and $p_0 = 10^5$ Pa can be found in [3]. In particular, the evolution in time of the contact surface speed is given. A value of ~ 4 km s^{-1} is obtained at 50 ns. Performing the ablation with an energy multiplied by a factor of 2 leads to an ablation rate (depth of the ablated layer) 50 % higher [26]. As a result, the ablated volume is higher and the energy per unit mass in the plasma as well as its pressure is almost unchanged. As a result, the expansion is more or less the same at $\bar{E}_1 = 10$ or 20 mJ. The present experimental results can then be compared from the expansion point of view with those obtained by the modeling at lower value of $\bar{E}_1$. The agreement is therefore satisfactory.

Moreover, comparing ROIs a and b for $H = 0$ mm for the N II transition, we can see that when the second pulse reaches the plasma, the increase in spectral radiance can also be observed later on the ROI a. This delay is approximately $\tau_{150} = 30$ ns for $\Delta t_{1-2} = 150$ ns, $\tau_{250} = 50$ ns for $\Delta t_{1-2} = 250$ ns and $\tau_{350} = 150$ ns for $\Delta t_{1-2} = 350$ ns. This means that the laser energy absorbed by the plasma at the center of ROI b does not remain on the optical axis, but diffuses around and in part toward the surface of the sample. This energy diffusion process takes place simultaneously with the electron diffusion according to a similar diffusion coefficient [36]. The time of diffusion increases when the absorbed energy is lower, therefore when the temperature and electron density reached after absorption are lower. This is an indirect proof of the better energy absorption within the plasma of the second laser pulse in higher density

conditions. Let us note l_{2-a} the distance between the location of the second optical axis and the upper limit of the ROI a when $H = 0$ mm (cf. figure 2). If we assume the delay $\tau_{\Delta t_{1-2}}$, the diffusion over l_{2-a} and the diffusion coefficient $D_{\Delta t_{1-2}}$ driven by the classical diffusion law

$$\tau_{\Delta t_{1-2}} \approx \frac{l_{2-a}^2}{D_{\Delta t_{1-2}}} \tag{1}$$

the diffusion coefficient $D_{\Delta t_{1-2}}$ consequently ranges between 1 and 5 $m^2\ s^{-1}$ approximately, according to the value of Δt_{1-2}. The distance l_{2-a} is 380 μm. These values are in satisfactory agreement with those determined either in plasmas at atmospheric pressure [37] or at low pressure [38] in similar conditions from the temperature point of view.

We can also note that this higher energy induced by the diffusion process leads to a higher spectral radiance for the Al I transitions for long time. Using the second pulse to increase the signals without additional ablation is therefore possible. Systematically, the spectral radiance for the Al I transitions is indeed higher over the ROI b than over the ROI a for acquisition times $t > 400$ ns. A ratio of a factor of 4 can be reached at $t = 850$ ns. This effect is also observed for the spectral radiance corresponding to the N II transition which is also globally increased by the absorption of the second pulse, but with a lower ratio.

We have deduced from figure 4 that the characteristic time scale of the plasma propagation from the sample to the position $z = 1.36$ mm is close to $t' = 320$ ns. As a result, producing an increase in the spectral radiance of the lines of interest with the second laser pulse should not be possible if $\Delta t_{1-2} < t'$ for $H = 1$ mm. Nevertheless, it is possible as illustrated by figures 5a and 5b. This apparent contradiction can be easily explained by the significant fluctuations of the plasma expansion. These

fluctuations are put in evidence by monitoring the spectral transmittivity of the aluminum plasma at each nanosecond pulse. These fluctuations are analyzed in section 3.4. The following comments then refer to the situations corresponding to an expansion fast enough to induce the absorption of the nanosecond pulse by the aluminum plasma for any value of Δt_{1-2} for $H = 1$ mm.

The ROI a is obviously too far from the second optical axis to be influenced by the energy absorption and diffusion. The time evolution of the ROI a is indeed the same for figures 5a, 5b and 5c in these conditions. Conversely, the ROI c exhibits strong modifications induced by the second pulse. A continuum is produced at $t = \Delta t_{1-2}$ and just after the absorption (continuum illustrated by figure 3b), the spectral radiance corresponding to the N II transition is higher than the one corresponding to the Al I transitions. Then the order is reversed. It is interesting to note that the spectral radiance of the Al I transitions at $t = 850$ ns becomes the same for the two ROIs. The energy of the second pulse absorbed by the plasma has therefore no influence for long times.

3.3. Electron density dynamics

The estimate of the electron density from the full width at half maximum (FWHM) can be obtained with the lines only when they are optically thin. When they are absorbed as the Al I resonance doublet (see section 3.2), other lines must be used.

Table 2 lists the different transitions and their characteristics exploited for the determination of n_e based on the FWHM. The additional lines with respect to the ones observed on figures 3b and 3c have been chosen because they significantly radiate. In table 2, the electron Stark broadening parameter ω_{ki} is listed. The related value is used to determine the electron density n_e from the comparison between the experimental full width at half maximum of the lines and the one classically given

by

$$\Delta\lambda_{ki}(n_e, T_e) = 2\,\omega_{ki}(T_e)\,\frac{n_e}{n_e^*} + \Delta\lambda_{ki}^{ionic}(n_e, T_e) \qquad (2)$$

In the previous equation, $\Delta\lambda_{ki}^{ionic}(n_e, T_e)$ is the ionic contribution to the Stark width and n_e^* is an electron density of reference (10^{22} m^{-3} for neutrals lines and 10^{23} m^{-3} for ionic lines) at which $\Delta\lambda_{ki}(n_e^*, T_e) = 2\,\omega_{ki}(T_e)$ with $\Delta\lambda_{ki}^{ionic}(n_e, T_e)$ negligible. The electron Stark broadening parameter $\omega_{ki}(T_e)$ weakly depends on the electron temperature T_e and has been considered here as independent.

With these data, we have derived the evolution in time of n_e obtained in the plasma produced by the picosecond laser pulse only. Figures 6a and 6b display this evolution. It is interesting to note that the results satisfactorily match the values predicted by our model CoRaM-Al implemented in an Eulerian code [3]. Indeed, in the conditions given in section 3.2, the calculated electron density reaches its maximum value of 2×10^{24} m^{-3} at time 90 ns and decreases to 5×10^{23} m^{-3} at time 500 ns. In addition, they are in very good agreement with the values reported recently by Cao *et al.* [39] in very similar conditions from the fluence point of view. In fact their values are weakly higher than ours since the fluence in their experiment is a bit higher. We have also measured this evolution when the second pulse is absorbed. This has been performed in the case $\Delta t_{1-2} = 150$ ns (experiments no 1 and 4) for which the density in the plasma is more significant than in the other conditions when the absorption takes place. This evolution is displayed on figures 6a and 6b for $H = 0$ mm and $H = 1$ mm, respectively. The uncertainty displayed on these figures results from the uncertainty in the determination of $\Delta\lambda_{ki}$ on the treated spectra. These evolutions have been also obtained for $\Delta t_{1-2} = 250$ and 350 ns. But, for the sake of clarity, only the maximum electron density just after the absorption

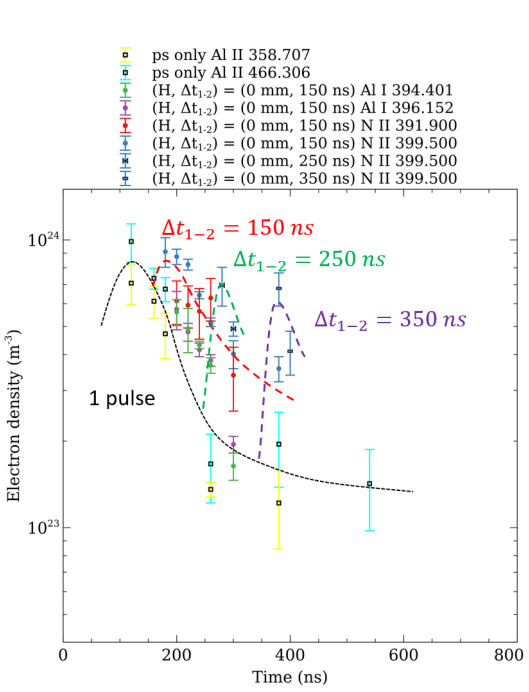

(a) $H = 0$ mm. Experiments no 1 ($\Delta t_{1-2} = 150$ ns), 2 ($\Delta t_{1-2} = 250$ ns) and 3 ($\Delta t_{1-2} = 350$ ns).

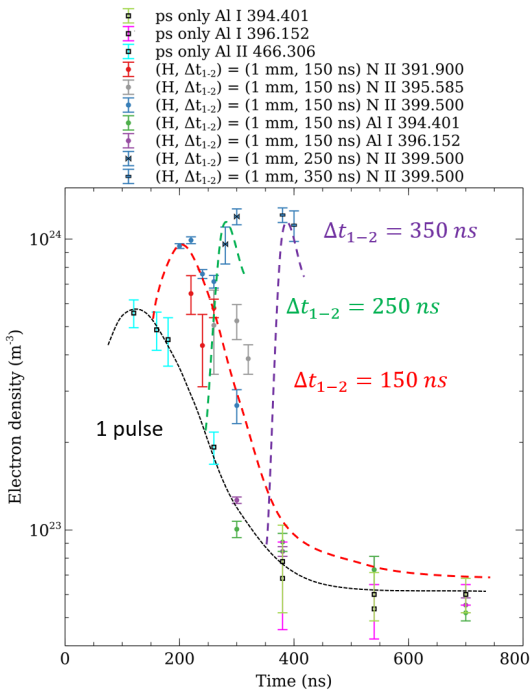

(b) $H = 1$ mm. Experiments no 4 ($\Delta t_{1-2} = 150$ ns), 5 ($\Delta t_{1-2} = 250$ ns) and 6 ($\Delta t_{1-2} = 350$ ns).

Figure 6: Time evolution of the electron density n_e (trends in colored dashed lines) and comparison with the evolution obtained without the second pulse (trends in thin dashed black lines).

has been indicated on figures 6a and 6b. We can observe that the absorption of the second pulse leads to the increase in n_e. The lower the initial density, the greater the variation. But this increase leads to almost the same maximum value $n_{e,max} \approx 10^{24}$ m^{-3}.

The increase in electron density results from MPI and from the collisional ionization enhanced by the increase in electron temperature by IB. This increase is obtained from the neutrals, ions and electrons already present in the plasma volume irradiated by the second laser pulse (cf. figure 2). As a result, the obtainable maximum electron density is a function of the temperature reached after the second pulse absorption period and of the reservoir of particles likely to be ionized. At the end of this ionization phase, the maximum Al^{2+}/Al^{+} density ratio is given by the Saha equilibrium equation [40]

$$\frac{[Al^{2+}]}{[Al^{+}]} = \frac{1}{n_e} \frac{2\, Z_{Al^{2+}}}{Z_{Al^{+}}} \left(\frac{2\pi\, m_e\, k_B\, T}{h^2} \right)^{3/2} e^{-\frac{E_i^{Al^{+}} - \Delta E}{k_B\, T}} \tag{3}$$

where $Z_{Al^{+}}$ and $Z_{Al^{2+}}$ are the partition function of Al^{+} and Al^{2+}, m_e the electron mass, k_B the Boltzmann constant, h the Planck constant, $E_i^{Al^{+}}$ the ionization potential of Al^{+} and ΔE the Al^{+} ionization potential lowering. Using the NIST database, the previous ratio has been calculated for $n_e = 10^{23}$ m^{-3} and 10^{24} m^{-3} as a function of T. The results are plotted on figure 7. The influence of the ionization potential lowering is weak because n_e is rather weak despite the values of T. Mainly, the values increase when T increases owing to the influence of the exponential term in equation (3). The curve corresponding to the case $n_e = 10^{23}$ m^{-3} is found under the curve corresponding to the case $n_e = 10^{24}$ m^{-3} because of the influence of the partition functions. The ionization potential of Al^{+} is significant with a value of 18.829 eV. This prevents this ratio to be higher than 10^{-2} at 100 000 K.

In a configuration similar to ours but with the use of optical fibers preventing any spatial characterization, Sobral *et al.* [41] have measured a weak increase in the temperature of around 1 500 K with $\bar{E}_2 = 100$ mJ, $f_2 = 150$ mm and $\lambda_2 = 1064$ nm when $(H, \Delta t_{1-2}) = (1$ mm, 500 ns). The temperature of the plasma where its radiation is maximum is then increased from around 15 500 K to 17 000 K. Since the (ionic) IB efficiency evolves as λ_2^3 [42], the effect on the plasma temperature of the laser absorption is necessary more significant than in our case. We can conclude that the temperature is too weak as demonstrated by figure 7 to induce a noticeable production of Al^{2+} ions. Thus the main ions are Al^+. Once all the Al atoms present in the volume irradiated by the second laser pulse are ionized, it is therefore impossible to further produce ions: the electron density n_e then reaches a saturation state.

From this point of view, it is valuable to further analyze the results of Sobral *et al.* They have exploited the broadening of the H_α line to derive the n_e values. Such a determination systematically leads to a weak overestimation of the derived electron density [43]. They have observed an increase in n_e from 9×10^{23} m^{-3} to 1.4×10^{24} m^{-3} due to the second laser pulse. Considering a reduction of n_e required by the use of the H_α line, the values are therefore in very good agreement with ours. Even if $\bar{E}_2$ is much higher than in our conditions, the increase in n_e and T_e are therefore close to our own results. This saturation effect is also observed.

All these results have important consequences. Indeed, we can conclude that the density of Al^{2+} remains negligible with respect to the one of Al^+ for a wide range of the second laser pulse energy. Since nitrogen is in much lower density within the plasma because its presence results from scattering elementary processes across the plasma boundary, its influence on the ionization state can be assumed as negligible. Anyway, this conclusion can be also deduced about nitrogen since the N^+ ionization potential is 29.601 eV. As a result, the absorption of the second pulse completes the

ionization of the plasma by forming only single charged ions. Due to the available neutrals and single charged ions already present in the plasma volume irradiated by the second pulse, the final ionization degree is then close to unity and cannot correspond to an electron density higher than $n_{e,max} \approx 10^{24}$ m^{-3} in the present case.

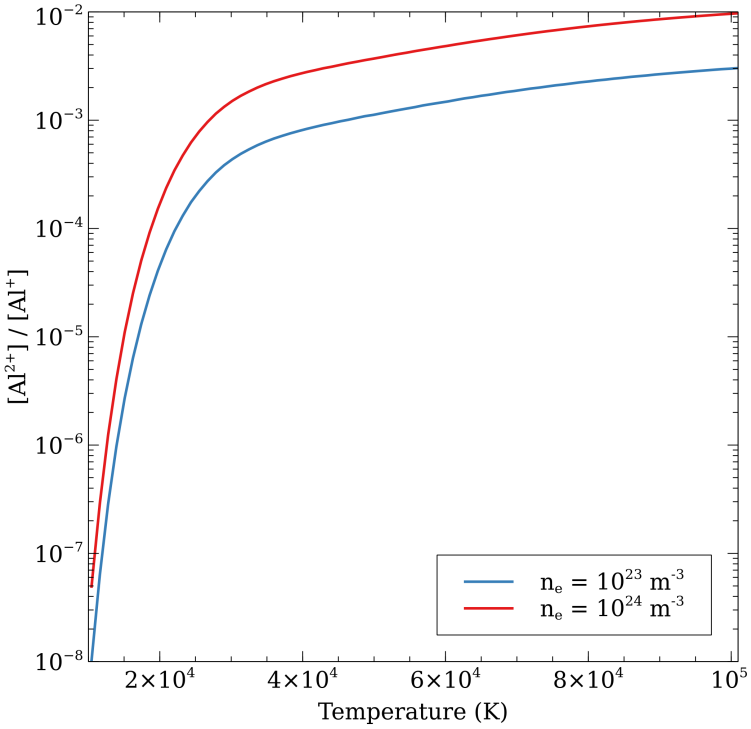

Figure 7: $[Al^{2+}]/[Al^{+}]$ density ratio as a function of temperature T at equilibrium for $n_e = 10^{23}$ m^{-3} (in blue) and for $n_e = 10^{24}$ m^{-3} (in red).

3.4. Spectral absorptivity measurements

In order to further characterize the plasma absorption, the energy of the second laser pulse is measured after the plasma crossing in the experimental conditions summarized in table 1. The results are plotted on figure 8. Between two experiments j each corresponding to $N^j \sim 2350$ pulses, the first laser pulse is not operated and the

aluminum plasma is therefore not produced. Then the second laser pulse propagates in ambient air without a significant breakdown formation. The measurement provided by the energy meter then leads to verify that the second laser source delivers pulses with almost steady mean energy.

The energy delivered by the second laser source is fluctuating (cf. section 2.1). The plasma absorption corresponds to nonlinear phenomena. As a result, the transmitted energy is fluctuating differently. Thus three mean values have been determined. The mean transmitted energy is denoted as $\bar{E}^j_{2,t}$. This value is indicated by a red segment on figure 8. Since the scattering of the laser light by the plasma is negligible in terms of energy [44], the mean spectral absorptivity $\bar{\alpha}_j = 1 - \frac{\bar{E}^j_{2,t}}{\bar{E}^j_2}$ is deduced where $\bar{E}^j_2$ is the mean value between before and after the experiment no j. Sometimes, other mean values rise because a great number of pulses correspond to a transmitted energy departing significantly from $\bar{E}^j_{2,t}$. Two additional mean values are then defined. The second mean value $\bar{E}^j_{2,t,max}$ is calculated from the pulses whose energy transmission is higher than $\bar{E}^j_{2,t}$. This corresponds to a minimum mean spectral absorptivity $\bar{\alpha}_{j,min} = 1 - \frac{\bar{E}^j_{2,t,max}}{\bar{E}^j_2}$ (blue segments in figure 8). The third mean value $\bar{E}^j_{2,t,min}$ is calculated from the pulses whose energy transmission is lower than $\bar{E}^j_{2,t}$. This corresponds to a maximum mean spectral absorptivity $\bar{\alpha}_{j,max} = 1 - \frac{\bar{E}^j_{2,t,min}}{\bar{E}^j_2}$ (green segments in figure 8).

We can observe that the pulse energy is significantly absorbed by the plasma. But the second pulse is never totally absorbed. Indeed, the lowest mean energy measured for the emerging pulse is 7.33 mJ (experiment no 1) for an incident value of $\bar{E}_2 = 15.49$ mJ. This corresponds to a mean spectral absorptivity of $\bar{\alpha}_1 = 0.53$. Since the density of the plasma decreases with time, the spectral absorptivity is lower when Δt_{1-2} is increased. Indeed, we see that for experiments 2 and 3, the mean value of the transmitted energy is higher, therefore the spectral absorptivity is lower. The

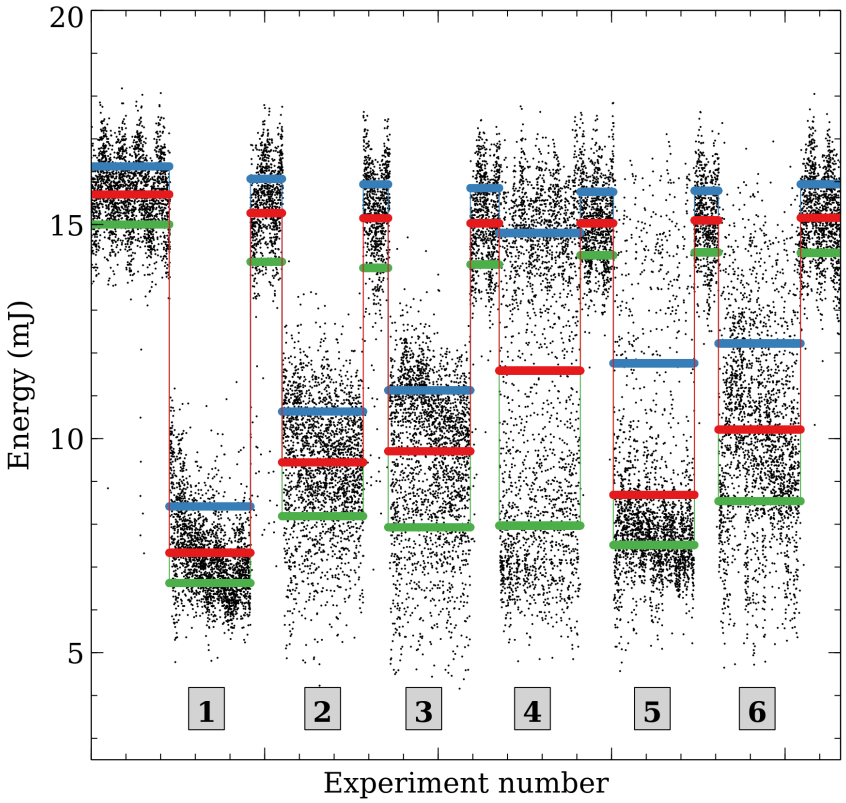

Figure 8: Energy of the second laser pulse emerging from the aluminum plasma region. Each black point corresponds to a laser pulse. The nominal energy is $\bar{E}_2 = 15.2$ mJ (cf. section 2.1) and is satisfactorily recovered between experiments. The transmitted energy is measured for each experimental condition listed in table 1. The mean values indicated by large segments have been obtained over ~ 2350 pulses. The blue segments correspond to mean values excluding pulses whose transmitted energy is lower than the red average and the green segments correspond to the complementary case.

mean spectral absorptivities are listed in table 3.

Experiment no j	1	2	3	4	5	6
$\bar{E}_2^j$ (mJ)	15.49	15.21	15.09	15.03	15.06	15.13
$\bar{E}_{2,max}^j$ (mJ)	16.21	16.00	15.89	15.81	15.78	15.87
$\bar{E}_{2,min}^j$ (mJ)	14.57	14.06	14.03	14.17	14.32	14.34
$\bar{E}_{2,t}^j$ (mJ)	7.33	9.45	9.71	11.59	8.69	10.21
$\bar{E}_{2,t,max}^j$ (mJ)	8.42	10.63	11.13	14.80	11.76	12.22
$\bar{E}_{2,t,min}^j$ (mJ)	6.63	8.19	7.93	7.97	7.51	8.54
N^j	2340	2340	2370	2340	2340	2370
N_{min}^j	920	1210	1320	1240	650	1080
N_{max}^j	1420	1130	1050	1100	1690	1290
$\bar{\alpha}_j$	0.53	0.38	0.36	0.23	0.42	0.33
$\bar{\alpha}_{j,min}$	0.46	0.30	0.26	0.02	0.22	0.19
$\bar{\alpha}_{j,max}$	0.57	0.46	0.48	0.47	0.50	0.44

Table 3: Mean energy incident to the plasma ($\bar{E}_2^j$, $\bar{E}_{2,min}^j$, $\bar{E}_{2,max}^j$), mean energy transmitted by the plasma ($\bar{E}_{2,t}^j$, $\bar{E}_{2,t,min}^j$, $\bar{E}_{2,t,max}^j$), number of pulses (N^j, N_{min}^j, N_{max}^j) and resulting spectral absorptivity ($\bar{\alpha}_j$, $\bar{\alpha}_{j,min}$, $\bar{\alpha}_{j,max}$) for the experiments of figure 8 performed in the conditions of table 1.

Experiments 4, 5 and 6 have been performed at a higher distance from the sample surface. Since an aluminum plasma produced by a picosecond laser pulse seems to be characterized by gradients as weak as in the case of a nanosecond laser-induced plasma [45], we should observe more or less the same experimental results as those observed for experiments 1, 2 and 3. Obviously, figure 8 shows that it is not the case except between experiments 3 and 6 despite the fluctuations. Indeed, we see in table 3 that the spectral absorptivity of the latter experiments is close to each other.

In addition, the fluctuations of experiments 4, 5 and 6 are much more significant than for experiments 1, 2 and 3. Besides the mean transmitted energy $\bar{E}^j_{2,t,max}$ for experiment 4 is almost equal to the mean transmitted energy $\bar{E}^j_2$ without plasma, and the mean transmitted energy $\bar{E}^j_{2,t,min}$ for experiment 4 is close to the mean energy $\bar{E}^j_{2,t}$ for experiment 1. These features are the direct result of the hypersonic expansion of the plasma put in evidence in section 3.2. Indeed, the laser pulse mainly interacts with the ambient atmosphere before the arrival of the plasma produced on the sample surface. In section 3.2, we have shown that the characteristic plasma expansion time over $z = 1.36$ mm is $t' = 320$ ns. This time is higher than $\Delta t_{1-2} = 150$ ns. The plasma should not have reached the position of the second laser pulse. Since the second laser fluence F_2 is lower than but very close to the air breakdown threshold, an air plasma is rarely produced. The transmitted energy $\bar{E}^4_{2,t,max} = 14.80$ mJ is therefore close to the one observed without aluminum plasma $\bar{E}^4_2 = 15.03$ mJ. Over the $N^4 = 2340$ pulses corresponding to experiment 4, $N^4_{min} = 1240$ pulses (i.e. 53 %) correspond to this situation and lead to $\bar{E}^4_{2,t,max} = 14.80$ mJ. Nevertheless, the second laser pulse often interacts with the aluminum plasma because of the fluctuations. This is the case for the other $N^4_{max} = 1100$ pulses (47 % of the total number of pulses) leading to a significant absorption. The resulting mean spectral absorptivity $\bar{\alpha}_{4,max} = 0.47$ is then close to the value $\bar{\alpha}_1 = 0.53$. The existence of these two complementary regimes is particularly obvious on figure 8. Indeed, two clouds of points are clarly observed around the mean values $\bar{E}^4_{2,min}$ and $\bar{E}^4_{2,max}$.

In the case of experiment 5, Δt_{1-2} is again lower than t'. Therefore the previous behaviour is still observed but in a reduced way. $N^5_{max} = 1690$ pulses lead to the mean spectral absorptivity $\bar{\alpha}_{5,max} = 0.50$ and $N^5_{min} = 650$ pulses lead to $\bar{\alpha}_{5,min} = 0.22$. For experiment 6, $\Delta t_{1-2} > t'$ and $N^6_{max} = 1290$ pulses lead to the mean spectral absorptivity $\bar{\alpha}_{6,max} = 0.44$ and $N^6_{min} = 1080$ pulses lead to $\bar{\alpha}_{6,min} = 0.19$.

In section 3.3, we have mentioned that the absorption of the second laser pulse by the aluminum plasma clearly illustrates a typical behaviour of saturation. Indeed, in any case the electron density reached by the plasma after absorption does not exceed around 10^{24} m^{-3}. This saturation-like situation is confirmed by the spectral absorptivity listed in table 3. Indeed, the reported values are never close to unity. The highest value for $\bar{\alpha}_j$ is 0.53. This means that the energy absorption is limited despite the high value energy available in the second laser pulse. Around 50 % of this energy crosses the plasma and does not interact with its particles.

4. Conclusion

A thorough study of the absorption of a nanosecond laser pulse at 532 nm by a picosecond laser-induced preformed aluminum plasma has been performed using a specific experimental device. The experiments have been carried out in air at atmospheric pressure. The absorption has been studied according to two parameters: the time delay between the plasma production and the time of absorption, and the location of the absorption with respect to the aluminum sample. The values of the electron density have been derived from the study of the Stark broadening of reliable ionic and atomic lines. We have observed that the absorption leads to a similar electron density of around 10^{24} m^{-3} for any starting value of the electron density. Absorptivity measurements have been also performed to quantitatively estimate the relationship between the increase in the electron density and the energy actually absorbed by the plasma. These measurements have put in evidence the strong fluctuations of this absorption due to those of the plasma propagation. The energy absorbed is at best of around 50 % of the incident energy. These results accredit the idea of a saturation of the absorption process due to the saturation of the production

of ions from atoms and ions already present in the plasma volume irradiated by the second pulse.

To verify this interpretation, similar measurements will be shortly performed at wavelengths 355 and 1064 nm in exactly the same configuration. Besides, these experiments will enable to verify that the energy is predominantly absorbed by inverse Bremsstrahlung. These measurements will be analyzed in the light of the modelling of the whole absorption process.

Acknowledgments

We thank the TRANSAT project funded by the Euratom Research and Training Programme 2014-2018 under grant agreement No 754586. This work has been carried out within the framework of the French Federation for Magnetic Fusion Studies (FR-FCM) and of the Eurofusion consortium, and has received funding from the Euratom research and training programme 2014-2018 and 2019-2020 under grant agreement No 633053. The views and opinions expressed herein do not necessarily reflect those of the European Commission. We also thank the *Agence Nationale de la Recherche* (ANR), through the program "*Investissement d'Avenir*" (ANR-10-LABX-09-01), LabEx EMC 3, PICOLIBS project and through the program "*Investissement d'Avenir*" (ANR-10-LABX-09-01), LabEx EMC 3, PTOLEMEE project. This work has been also partially financed by the "Region Normandie", France and the European Regional Development Fund (ERDF) of the European Union, ZEOMETHYL project.

Declaration of interest

None

Credit author statement

Aurélien Favre: investigation, writing

Vincent Morel: supervision

Arnaud Bultel: supervision, writing

Gilles Godard: resources

Said Idlahcen: resources

Christian Grisolia: resources

References

[1] A.W. Miziolek, V. Palleschi, I. Schechter (2006) Laser-Induced Breakdown Spectroscopy (LIBS) Fundamentals and Applications, Cambridge University Press.

[2] D.I. Rosen, D.E. Hastings, G.M. Weyl (1982) Coupling of pulsed 0.35 μm laser radiation to titanium alloys, J. Appl. Phys. 53 8, 5882-5890. Doi: 10.1063/1.331429

[3] V. Morel, A. Bultel, J. Annaloro, C. Chambrelan, G. Edouard, C. Grisolia (2015) Dynamics of a femtosecond/picosecond laser-induced aluminum plasma out of thermodynamic equilibrium in a nitrogen background gas, Spectrochim. Acta Part B 103-104: 112-123. Doi:10.1016/j.sab.2014.11.014

[4] M. Boueri, M. Baudelet, J. Yu, X. Mao, S.S. Mao, R. Russo (2009) Early stage expansion and time-resolved spectral emission of laser-induced plasma from polymer, Appl. Surf. Sci. 255, 9566-9571. Doi: 10.1016/j.apsusc.2009.04.088

[5] A. Semerok, C. Dutouquet (2004) Ultrashort double pulse laser ablation of metals, Thin Solid Films 453-454: 501-505. Doi: 10.1016/j.tsf.2003.11.115

[6] J. Hermann, C. Vivien, A.P. Carricato, C. Boulmer-Leborgne (1998) A spectroscopic study of laser ablation plasma from Ti, Al and C, Appl. Surf. Sci. 127-129, 645-649. Doi: 10.1016/S0169-4332(97)00719-8

[7] J.-B. Sirven, B. Bousquet, L. Canioni, L. Sarger (2004) Time-resolved and time-integrated single-shot laser-induced plasma experiments using nanosecond and femtosecond laser pulses, Spectrochim. Acta Part B 59, 1033-1039. Doi: 10.1016/j.sab.2004.05.009

[8] Y. He, X. Liu, Y. Lv, F. Liu, J. Peng, T. Shen, Y. Zhao, Y. Tang, S. Luo (2018) Quantitative analysis of nutrient elements in soil using single and double-pulse laser-induced breakdown spectroscopy, Sensors 18, 1526. Doi: 10.3390/s18051526

[9] C.R. Bhatt, D. Hartzler, J.C. Jain, D.L. McIntyre (2020) Evaluation of analytical performance of double pulse laser-induced breakdown spectroscopy for the detection of rare earth elements, Optics and Laser Technology 126, 106110. Doi: /10.1016/j.optlastec.2020.106110

[10] M. Cui, Y. Deguchi, Z. Wang, S. Tanaka, Y. Fujita, S. Zhao (2019) Improved analysis of manganese in steel samples using collinear long-short double pulse laser-induced breakdown spectroscopy (LIBS), Applied Spectroscopy 73, 152-162. Doi: 10.1177/0003702818803943

[11] D. Sun, Y. Ma, Y. Wang, M. Su, Q. Lu, C. Dong (2018) Limits of detection for aluminum-based alloys by spatially resolved single- and double-pulse laser-induced breakdown spectroscopy, Anal. Methods Doi: 10.1039/C8AY00596F

[12] H. Shakeel, S.U. Haq, Q. Abbas, A. Nadeem, V. Palleschi(2018) Quantitative analysis of Ge/Si alloys using double-pulse calibration-free laser-induced breakdown spectroscopy, Spectrochim. Acta Part B 146, 101-105. Doi: 10.1016/j.sab.2018.05.008

[13] G. Nicolodelli, P.R. Villas-Boas, C.R. Menegatti, G.S. Senesi, D.V. Magalhaes, D. De Souza, B.M.B.P. Milori, B.S. Marangoni (2018) Determination of Pb in soils by double-pulse laser-induced breakdown spectroscopy assisted by continuum wave-diode laser-induced fluorescence, Appl. Optics 57, 8366-8372. Doi: 10.1364/AO.57.008366

[14] S. Zhao, C. Song, X. Gao, J. Lin (2019) Quantitative analysis of Pb in soil by femtosecond-nanosecond double-pulse laser-induced breakdown spectroscopy, Results in Physics 15, 102736. Doi: 10.1016/j.rinp.2019.102736

[15] Y. Wang, A. Chen, Q. Wang, D. Zhang, S. Li, Y. Jiang, M. Jin (2020) Study of signal enhancement in collinear femtosecond-nanosecond doublepulse laser-induced breakdown spectroscopy, Optics and Laser Technology 122, 105587. Doi: 10.1016/j.optlastec.2019.105887

[16] X. Xiao, S. Le Berre, D.G. Fobar, M. Burger, P.J. Skrodzki, K.C. Hartig, A.T. Motta, I. Jovanovic (2018) Measurement of chlorine concentration on steel surfaces via fiber-optic laser-induced breakdown spectroscopy in double-pulse configuration, Spectrochim. Acta Part B 141, 44-52. Doi: 10.1016/j.sab.2018.01.003

[17] Z. Tang, R. Zhou, Z. Hao, S. Ma, W. Zhang, K. Liu, X. Li, X. Zeng, Y. Lu (2019) Micro-destructive analysis with high sensitivity using double-pulse resonant laser-induced breakdown spectroscopy, J. Anal. At. Spectrom. Doi: 10.1039/C9JA00072K

[18] A. De Giacomo, A. De Bonis, M. Dell'Aglio, O. De Pasquale, R. Gaudiuso, S. Orlando, A. Santagata, G.S. Senesi, F. Taccogna, R. Teghil (2011) Laser ablation of graphite in water in a range of pressure from 1 to 146 atm using signle and double pulse techniques for the production of carbon nanostructures, J. Phys. Chem. C 115, 5123-5130. Doi: 10.1021/jp109389c

[19] A. De Giacomo, M. Dell'Aglio, D. Bruno, R. Gaudiuso, O. De Pascale (2008) Experimental and theoretical comparison of single-pulse and double-pulse laser induced breakdown spectroscopy on metallic samples, Spectrochim. Acta Part B 63, 805-816. Doi: 10.1016/j.sab.2008.05.002

[20] M. Corsi, G. Cristoforetti, M. Giuffrida, M. Hidalgo, S. Legnaioli, V. Palleschi, A. Salvetti, E. Tognoni, C. Vallebona (2004) Three-dimensional analysis of laser induced plasmas in single and double pulse configuration, Spectrochim. Acta Part B 59, 723-735. Doi: 10.1016/j.sab.2004.02.001

[21] P.A. Benedetti, G. Cristoforetti, S. Legnaioli, V. Palleschi, L. Pardini, A. Salvetti, E. Tognoni (2005) Effect of laser pulse energies in laser induced breakdown spectroscopy in double-pulse configuration, Spectrochim. Acta Part B 60, 1392-1401. Doi: 10.1016/j.sab.2005.08.007

[22] G. Cristoforetti, S. Legnaioli, V. Palleschi, A. Salvetti, E. Tognoni (2004) Influence of ambient gas pressure on laser-induced breakdown spectroscopy technique in the parallel double-pulse configuration, Spectrochim. Acta Part B 59, 1907-1917. Doi: 10.1016/j.sab.2004.09.003

[23] E. Tognoni, G. Cristoforetti (2014) Basic mechanisms of signal enhancement in ns double-pulse laser-induced breakdown spectroscopy in gas environment, J. Anal. At. Spectrom., 2014,29, 1318-1338. Doi: 10.1039/C4JA00033A

[24] A. Bogaerts, Z. Chen, D. Autrique (2008) Double pulse laser ablation and laser induced breakdown spectroscopy: a modeling investigation, Spectrochim. Acta Part B 63, 746-754. Doi: 10.1016/j.sab.2008.04.005

[25] Y. Nosrati, S.H. Tavasoli, M.M. Hassanimatin, A. Safi (2020) Study of material ablation and plasma radiation in double-pulse laser induced breakdown spectroscopy at different delay times: Modeling and numerical simulation, Phys. Plasmas 27, 023301. Doi: 10.1063/1.5132804

[26] A. Bultel, V. Morel, A. Favre, G. Godard, A. Benyagoub, I. Monnet, A. Semerok, M. Dinescu, S. Markelj, P. Magaud, C. Grisolia, Towards ps-LIBS tritium measurements in W/Al materials, Fusion Engineering and Design, Volume 146, Part B, 2019, Pages 1971-1974, ISSN 0920-3796, Doi: 10.1016/j.fusengdes.2019.03.079.

[27] J. Scaffidi, W. Pearman, J. C. Carter, S. M. Angel (2006) Observations in collinear femtosecond-nanosecond dual-pulse laser-induced breakdown spectroscopy, Appl.Spectrosc., 60, 65. Doi: 10.1366/000370206775382857

[28] H. Amamou, A. Bois, B. Ferhat, R. Redon, B. Rossetto, M. Ripert (2003) Correction of the self-absorption for reversed spectral lines: application to two resonance lines of neutral aluminium, J. Quant. Spectrosc. Radiat. Transfer 372, 365-372. Doi: 10.1016/S0022-4073(02)00163-2

[29] D.M. Surmick and C.G. Parriger (2015) Self-absorption corrections to hydrogen and aluminum line profiles in laser-induced plasma, International Review of Atomic and Molecular Physics 6, 101-115. International Science Press, ISSN: 2229-3159

[30] M. Cirisan, M. Cvejic, M.R. Gavrilovic, S. Jovicevic, N. Konjevic, J. Hermann (2014) Stark broadening measurement of Al II lines in a laser-induced plasma, J. Quant. Spectrosc. Tranfer 133, 652-662. Doi: 10.1016/j.jqsrt.2013.10.002

[31] N. Konjevic, A. Lesage, J.R. Fuhr, W.L. Wiese (2002) Experimental Stark Widths and Shifts for Spectral Lines of Neutral and Ionized Atoms (A Critical Review of Selected Data for the Period 1989 Through 2000), Journal of Physical and Chemical Reference Data 31, 819-927. Doi: 10.1063/1.1486456

[32] H.R. Griem (1974) Spectral Line Broadening by Plasmas, McGraw Hill, New York, Pages 320-378.

[33] A.W. Allen, M. Blaha, W.W. Jones, A. Sanchez, H.R. Griem (1975) Stark-broadening measurement and calculations for a singly ionized aluminum line, Phys. Rev. A 11, 477. Doi: 10.1103/PhysRevA.11.477

[34] Kramida, A., Ralchenko, Yu., Reader, J., and NIST ASD Team (2019). NIST Atomic Spectra Database (ver. 5.7.1), [Online]. Available: https://physics.nist.gov/asd [2019, December]. National Institute of Standards and Technology, Gaithersburg, MD. Doi: 10.18434/T4W30F

[35] K. B. S. Eriksson and H. B. S. Isberg, The Spectrum of Atomic Aluminium, Al I, Ark. Fys. (Stockholm) 23(47), 527-542 (1963)

[36] M. Okabayashi (1973) Heating Mechanism, Electron Thermal Conductivity and Particle Diffusion Coefficient in High Electron Temperature Plasma Produced by High Power Microwave Heating in the FM-1 Spherat, Sixth Enropean Conference on Controlled Fusion and Plasma Physics, Moscow.

[37] G.J.M. Hagelaar, L.C. Pitchford (2005) Solving the Boltzmann equation to obtain electron transport coefficients and rate coefficients for fluid models, Plasma Sources Sci. Technol. 14, 722-733. Doi: 10.1088/0963-0252/14/4/011

[38] M. Ghoranneviss, S. Meshkani, M. Lafouti (2017) Different techniques for investigation of plasma diffusion coefficient in IR-TI tokamak, AIP Conference Proceedings 1824, 020003. Doi: 10.1063/1.4978816

[39] S. Cao, M. Su, P. Ma, K. Wang, Q. Min, D. Sun, R. Cheng, T. Ying, C. Dong (2020) Expansion dynamics and emission characteristics of nanosecond-picosecond collinear double pulse laser-induced Al plasma in air, J. Quant. Spectrosc. Radiat. Transfer 242, 106773. Doi: 10.1016/j.jqsrt.2019.106773

[40] G.E. Rolader, J.H. Batteh, P.V. Desai (1988) Comparison of partition function calculations for metal plasmas, J. Appl. Phys. 64, 1101-1107. Doi: 10.1063/1.342506

[41] H. Sobral, R. Sangines (2014) Comparison of plasma parameters and line emissions of laser-induced plasmas of an aluminum target using singnle and orthogonal double nanosecond/picosecond pulses, Spectrocim. Acta Part B 94-95, 1-6. Doi: /10.1016/j.sab.2014.02.002

[42] V. Morel, A. Bultel (2014) Theoretical study of the formation mechanism of laser-induced aluminum plasmas using Nd:YAG fundamental, second and third harmonics, Spectrochim. Acta Part B 94-95, 63-70. Doi: 10.1016/j.sab.2014.03.003

[43] Z. Mijatovic, S. Djurovic, L. Gavanski, T. Gajo, A. Favre, V. Morel, A. Bultel (2020) Plasma density determination by using hydrogen Balmer H_α spec-

664 tral line with improved accuracy, Spectrochim. Acta Part B 166, 105821. Doi:
665 10.1016/j.sab.2020.105821

666 [44] E. Schwartz, S. Gross, B. Fischer, I. Muri, J. Tauer, H. Kofler, E. Winter (2010)
667 Laser-induced optical breakdown applied for laser spark ignition, Laser and
668 Particle Beams 28, 109-119. Doi: 10.1017/S0263034609990668

669 [45] S. Laville, F. Vidal, T.W. Johnston, M. Chaker, B. Le Drogoff (2004) Modeling
670 the time evolution of laser-induced plasmas for various pulse durations and
671 fluences, Phys. Plasmas 11, 2182-2190. Doi: 10.1063/1.1691454

Arnaud BULTEL
Associate Professor
CORIA UMR 6614
Normandie Université
CNRS – Université et INSA de Rouen
Campus universitaire du Madrillet
76800 Saint-Étienne du Rouvray
FRANCE

June, 13tn, 2020

GRAPHICAL ABSTRACT

Figure 1: Schematic view of the platform PLEIADES.
The first laser source on the left produces infrared photons along the red axis. After focus, the plasma in yellow is generated on the Al sample placed on the central (xyz)-stage holder. The second laser source in the background produces visible photons along the green axis. They are focused in the plasma whose spectroscopic analysis is performed by the spectrometer on the purple axis.

Figure 2: Relative sensor/plasma arrangement in the case where the second optical axis corresponds to the location of ROI c (H = 1 mm). When H = 0 mm, the distance betwen the upper border of the ROI a and the second optical axis is $l_{2\text{-}a}$.

Figure 3: ROIs and associated spectra for λ ~ 396 nm at the acquisition time 40, 380 and 480 ns after the production of the plasma by the first pulse at t = 0. The plasma is reheated by the second pulse in the conditions (H; $\Delta t_{1\text{-}2}$) = (1 mm, 350 ns) of the experiment no 6. The red frames and spectra correspond to the plasma close to the sample (ROI a). The yellow frames and spectra correspond to the plasma reheated by the second pulse (ROI c).

Figure 4: Time evolution of the spectral radiance at the wavelength of the Al I and N II transitions of figure 3 obtained without second pulse close to the sample's surface (ROI a, continuous lines) and ~ 1 mm above (ROI c, dashed lines).

Figure 5: Time evolution of the spectral radiance at the wavelength of the Al I and N II transitions obtained close to the sample's surface (ROI a, continuous lines) and over the ROI corresponding to the position of the second pulse (dashed lines, ROI b for H = 0 mm and ROI c for H = 1 mm) for the different values of $\Delta t_{1\text{-}2}$ (colors similar to figure 4).

Figure 6: Time evolution of the electron density n_e (trends in colored dashed lines) and comparison with the evolution obtained without the second pulse (trends in thin dashed black lines).

Figure 7: $[Al^{2+}]$=$[Al^{+}]$ density ratio as a function of temperature T at equilibrium for $n_e = 10^{23}$ m^{-3} (in blue) and for $n_e = 10^{24}$ m^{-3} (in red).

Figure 8: Energy of the second laser pulse emerging from the aluminum plasma region. Each black point corresponds to a laser pulse. The nominal energy is $E_2 = 15.2$ mJ (cf. section 2.1) and is satisfactorily recovered between experiments. The transmitted energy is measured for each experimental condition listed in table 1. The mean values indicated by large segments have been obtained over ~ 2350 pulses. The blue segments correspond to mean values excluding pulses whose transmitted energy is lower than the red average and the green segments correspond to the complementary case.